

Neural-Guided Domain Restriction to Accelerate Pseudospectra Computation for Structured Non-normal Banded Matrices

Amit Punia¹Rakesh Kumar^{2*}Madan Lal³

¹Jai Narain Vyas University, Jodhpur, Rajasthan, India
Email: amitpunia.maths@gmail.com

²SRM University-AP, Amaravati, Andhra Pradesh, India
Email: r.k.dhiman.math@gmail.com

³Jai Narain Vyas University, Jodhpur, Rajasthan, India
Email: madan.lakhani288@gmail.com

Abstract

Computing pseudospectra of non-normal matrices is essential for understanding the stability and transient behavior of dynamical systems. Such analysis is critical in applications including fluid dynamics, control systems, and differential operators, where non-normality can lead to significant transient amplification and sensitivity to perturbations that are not captured by eigenvalue analysis alone. At large scales, commonly used numerical approaches for pseudospectra computation can become computationally demanding, as they require repeated auxiliary computations to identify spectrally sensitive regions in the complex plane.

We present a neural network-based approach that predicts sensitive regions directly from matrix features, thereby avoiding exhaustive pseudospectra evaluation across the entire complex plane. We calibrate the prediction threshold on validation data to ensure reliable coverage of sensitive regions. The trained neural network guides the selection of grid points requiring full computation, enabling focused computation only where necessary. The approach provides a practical preprocessing strategy for efficient pseudospectra computation. Numerical experiments on non-normal banded matrices demonstrate substantial speedup compared to full grid-based numerical evaluation while maintaining high accuracy in identifying sensitive regions.

Keywords. Pseudospectra, Non-normal matrices, Neural networks, Spectral analysis, Adaptive methods, Banded matrices

AMS subject classification. 15A18, 65F15, 68T07, 47A10

*Corresponding author. Email: r.k.dhiman.math@gmail.com

1 Introduction

For a comprehensive understanding of physical models in science and engineering, the formulation of an appropriate mathematical model is essential. Valuable insights into system behavior can often be obtained from the eigenvalues or spectrum of the governing operator, highlighting their fundamental role in both theoretical and applied mathematics. In general, eigenvalues provide insight into algorithmic behavior, physical phenomena, and the qualitative structure of dynamical systems [1]. They are widely used across diverse fields including quantum mechanics, structural mechanics, fluid dynamics, numerical analysis, and probability theory, where they help characterize stability, asymptotic behavior, and rates of convergence or divergence.

Despite their importance, eigenvalues alone are often insufficient to describe the behavior of non-normal operators. Several models in fluid mechanics, such as the instability of magnetic plasmas, the formation of cyclones, and fluid flow in circular pipes, demonstrate the limitations of eigenvalue-based analysis [2]. A classical example is the pipe Poiseuille flow problem, where the flow remains smooth at low velocities but transitions to turbulence at higher velocities [3, 4, 5]. In such cases, eigenvalue analysis fails to explain experimentally observed instabilities. In contrast, pseudospectral analysis captures transient growth and sensitivity effects, thereby providing a more accurate description of system behavior.

Pseudospectra also play a crucial role in numerical analysis. They provide valuable insight into stiffness, numerical instability of discretized differential equations, and the convergence behavior of iterative methods for non-symmetric matrix problems [2, 6, 7, 8]. These phenomena are closely linked to the non-normality of the underlying operators, where even small perturbations can lead to significant changes in system dynamics.

In general, non-normal and non-Hermitian problems exhibit behavior that cannot be fully characterized by eigenvalues alone. Such systems require a more refined analytical framework, where pseudospectra provide deeper insight into stability, sensitivity, and transient dynamics. Applications such as optical wave propagation further illustrate this sensitivity in complex media [9].

Recent advances in machine learning (ML) and artificial intelligence (AI) have demonstrated strong performance in high-dimensional approximation, surrogate modeling, and data-driven scientific computing [10, 11, 12]. These approaches are particularly effective in problems where analytical characterization is challenging, such as non-self-adjoint eigenvalue problems in numerical linear algebra. Such problems are highly sensitive to perturbations, often leading to spectral pollution, transient growth, and numerical instabilities.

Unlike self-adjoint systems, which are supported by well-established theoretical frameworks such as Sturm–Liouville theory [13], non-self-adjoint operators do not admit a similarly complete theory [2]. This gap motivates the development of hybrid computational approaches that combine data-driven learning with classical numerical methods.

To address these challenges, we propose a scalable and interpretable hybrid framework for predicting pseudospectral behavior. The approach integrates neural network-based prediction with selective singular value computations to identify regions of spectral sensitivity efficiently. By leveraging the pattern recognition capabilities of neural networks, the proposed method reduces the computational burden associated with full-grid pseudospectra evaluation while preserving essential spectral features.

To generate accurate training data, we employ the exclusion-region singular-value method, which is closely related to established pseudospectra computation techniques based on selective singular value evaluation [14, 15]. This approach ensures that the minimum singular value is computed exactly at relevant grid points, thereby providing reliable and physically consistent labels for training. Moreover, it preserves fine pseudospectral structures, such as sharp sensitivity regions and localized features near eigenvalues, which are essential for capturing subtle instability mechanisms in non-normal systems.

The computational efficiency of this approach enables the construction of large and diverse datasets consisting of thousands of random matrices and their corresponding pseudospectra. Such datasets are crucial for training robust machine learning models and mitigating overfitting. To the best of our knowledge, relatively limited work exists on directly predicting matrix pseudospectra using deep learning. However, recent advances in scientific machine learning and operator learning suggest that data-driven approaches can effectively approximate complex operator-dependent mappings [11, 12].

Contributions of this work are as follows:

- We propose a hybrid data-driven framework for efficient approximation of pseudospectra in non-normal matrices.
- We develop a neural network-based predictor to identify regions of spectral sensitivity, significantly reducing the number of required singular value computations.
- We design a data generation strategy based on selective singular value evaluation to produce accurate and physically consistent training labels.
- We introduce a hierarchical coarse-to-fine prediction strategy to reduce the number of neural network evaluations.
- We demonstrate substantial computational speedup while maintaining high accuracy through extensive numerical experiments.

The remainder of this paper is organized as follows. Section 2 introduces the mathematical foundations of pseudospectra, Section 3 presents the proposed neural network framework, Section 4 details the hybrid computational strategy, and Section 5 reports numerical experiments and performance evaluation. Finally, Sections 6 and 7 provide discussion and concluding remarks.

2 Preliminaries

For a matrix $\mathbf{A} \in \mathbb{C}^{n \times n}$, the *pseudospectra* characterize the behavior of linear systems beyond what eigenvalues alone reveal. While eigenvalues determine asymptotic stability, pseudospectra govern transient dynamics and sensitivity to perturbations [2]. This is particularly critical for non-normal matrices, where $\mathbf{A}\mathbf{A}^* \neq \mathbf{A}^*\mathbf{A}$, which arise in fluid dynamics [4], control theory [3, 16], and weather prediction [17].

For non-normal matrices, the eigenvectors may fail to form a complete or orthogonal basis. Moreover, the eigenvector matrix can be highly ill-conditioned, indicating strong sensitivity of the system to even very small perturbations.

As illustrated in Fig. 1, for normal operators, the ϵ -pseudospectrum $\Lambda_\epsilon(A)$ consists of points in \mathbb{C} that lie within a distance ϵ of the spectrum $\sigma(A)$. In contrast, for non-normal operators, $\Lambda_\epsilon(A)$ can extend far beyond the eigenvalue locations, reflecting increased spectral sensitivity.

Consider the Jordan block matrix A of order 32 with ones on the subdiagonal. All its eigenvalues are zero. However, even a small perturbation in a single entry of the first row of A drastically affects the eigenvalues, as illustrated in Fig. 2. The eigenvalues of the perturbed matrix B spread away from the origin and lie approximately on a circle centered at zero. Furthermore, Fig. 3 shows the distribution of eigenvalues under ten thousand random perturbations of the entries of A .

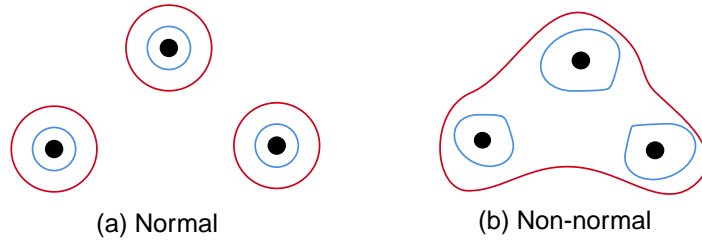


Figure 1: Effect of perturbation on normal and non-normal matrix eigenvalues

$$A = \begin{bmatrix} 0 & 0 & 0 & 0 & 0 \\ 1 & 0 & 0 & 0 & 0 \\ 0 & 1 & 0 & 0 & 0 \\ 0 & 0 & 1 & 0 & 0 \\ 0 & 0 & 0 & 1 & 0 \end{bmatrix}_{32}$$

$$B = \begin{bmatrix} 0 & 0 & 0 & 0 & 0.01 \\ 1 & 0 & 0 & 0 & 0 \\ 0 & 1 & 0 & 0 & 0 \\ 0 & 0 & 1 & 0 & 0 \\ 0 & 0 & 0 & 1 & 0 \end{bmatrix}_{32}$$

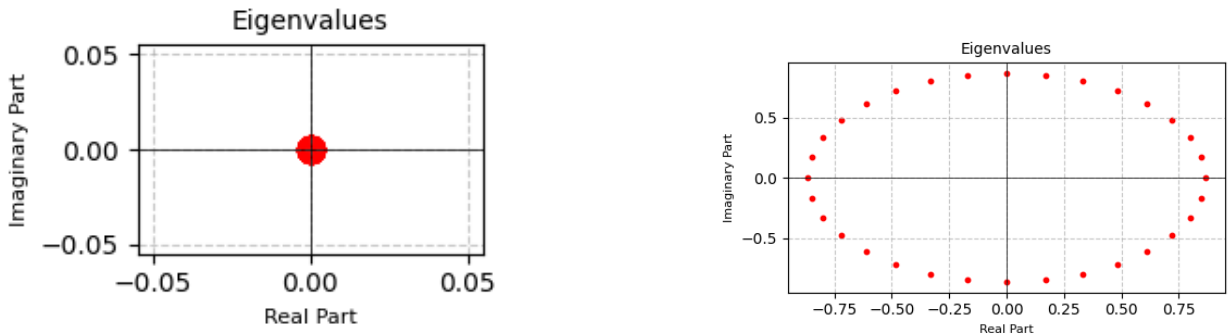


Figure 2: Effect of a perturbation on the eigenvalues of matrix A

These observations demonstrate that eigenvalues and eigenvectors alone are insufficient for analyzing non-normal matrices. The pseudospectrum, or ϵ -spectrum, is defined as the set of all eigenvalues of \mathbf{A} and those of nearby perturbed matrices [2]. When dealing with highly non-normal problems, pseudospectral analysis is more reliable, as eigenvalue-based analysis may be insufficient.

Consider the dynamical system:

$$\frac{d\mathbf{x}}{dt} = \mathbf{A}\mathbf{x}. \quad (1)$$

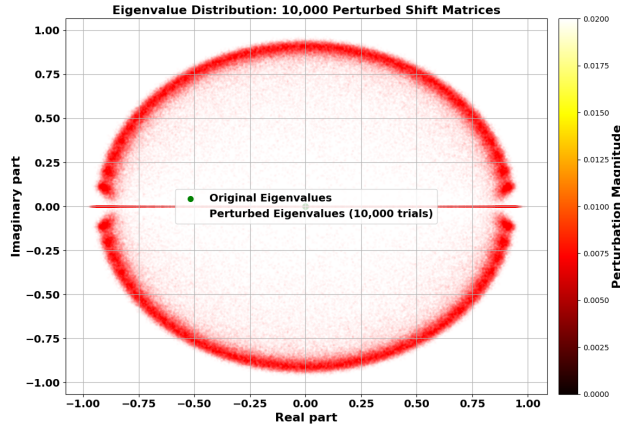


Figure 3: Distribution of eigenvalues under random perturbations

Even when all eigenvalues of \mathbf{A} have negative real parts, non-normality can cause large transient growth before eventual decay. Classical eigenvalue analysis fails to capture this behavior, motivating the use of pseudospectral analysis.

Definition 2.1 (Resolvent Norm). For a matrix \mathbf{A} , the resolvent is defined as $(z\mathbf{I} - \mathbf{A})^{-1}$ for $z \notin \sigma(\mathbf{A})$. If \mathbf{A} is normal, then

$$\|(z\mathbf{I} - \mathbf{A})^{-1}\| = \frac{1}{\text{dist}(z, \sigma(\mathbf{A}))}.$$

Remark. For non-normal matrices, the resolvent norm may significantly deviate from $\frac{1}{\text{dist}(z, \sigma(\mathbf{A}))}$, reflecting high spectral sensitivity.

Definition 2.2 (Pseudospectrum). [1, 2] For $\mathbf{A} \in \mathbb{C}^{n \times n}$ and $\epsilon > 0$, the ϵ -pseudospectrum is defined as

$$\begin{aligned} \Lambda_\epsilon(\mathbf{A}) &= \left\{ z \in \mathbb{C} : \|(z\mathbf{I} - \mathbf{A})^{-1}\| \geq \frac{1}{\epsilon} \right\} \\ &= \bigcup_{\|\mathbf{E}\| \leq \epsilon} \lambda(\mathbf{A} + \mathbf{E}) \\ &= \{ z \in \mathbb{C} : \sigma_{\min}(z\mathbf{I} - \mathbf{A}) \leq \epsilon \}. \end{aligned} \tag{2}$$

Here, $\lambda(\cdot)$ denotes the spectrum and $\sigma_{\min}(\cdot)$ denotes the smallest singular value.

The second characterization shows that $\Lambda_\epsilon(\mathbf{A})$ contains all eigenvalues of matrices within an ϵ -neighborhood of \mathbf{A} , thereby quantifying spectral sensitivity.

Remark (Non-normality and Spectral Sensitivity). For normal matrices, the pseudospectra consist of ϵ -disks centered at eigenvalues. For non-normal matrices, $\Lambda_\epsilon(\mathbf{A})$ can extend far beyond the eigenvalue locations, indicating strong sensitivity to perturbations [1, 4].

2.1 Singular Value Decomposition

The standard approach to computing pseudospectra discretizes the complex plane on a rectangular grid

$$\mathcal{G} = \{z_{ij} : i = 1, \dots, N_y, j = 1, \dots, N_x\},$$

where

$$z_{ij} = x_j + iy_i, \quad x_j \in [a, b], \quad y_i \in [c, d],$$

for a domain $[a, b] \times [c, d] \subset \mathbb{C}$ covering the region of interest.

For each grid point $z \in \mathcal{G}$, we compute

$$\sigma_{\min}(z) = \sigma_{\min}(zI - A)$$

via the singular value decomposition (SVD), which forms the basis of standard pseudospectra computation methods [2, 14, 18, 19].

If $zI - A = U\Sigma V^*$ is the SVD, where $\Sigma = \text{diag}(\sigma_1, \dots, \sigma_n)$ with $\sigma_1 \geq \dots \geq \sigma_n \geq 0$, then $\sigma_{\min}(z) = \sigma_n$.

The region of interest, referred to as the *sensitive zone*, is defined as

$$\mathcal{S}_\varepsilon = \{z \in \mathcal{G} : \sigma_{\min}(z) \leq \varepsilon\}. \quad (3)$$

Visualization typically uses contour plots of $\log_{10}(\sigma_{\min}(z))$, where the level curve $\log_{10}(\varepsilon)$ approximates the pseudospectrum boundary.

2.2 Computational Cost Analysis

The primary computational bottleneck in pseudospectra computation arises from repeated singular value decomposition (SVD) evaluations, as observed in large-scale algorithms [14]. For a matrix $A \in \mathbb{C}^{n \times n}$ and a grid \mathcal{G} with $N = N_x \times N_y$ points, the total computational cost is

$$\mathcal{C}_{\text{full}} = N \cdot \mathcal{C}_{\text{SVD}}(n), \quad (4)$$

where $\mathcal{C}_{\text{SVD}}(n)$ denotes the cost of a single SVD.

Using standard algorithms (e.g., Golub–Reinsch or divide-and-conquer methods), the cost scales as $\mathcal{C}_{\text{SVD}}(n) = O(n^3)$ floating-point operations [20].

For typical grid sizes ($N = 10^4$) and moderate matrix dimensions (e.g., $n = 64$), the total computational cost is on the order of 10^9 floating-point operations, which becomes prohibitive for larger problems.

A key observation is that the sensitive region \mathcal{S}_ε typically occupies only a small fraction of the grid. Let $\rho = |\mathcal{S}_\varepsilon|/N$. If this region could be identified *a priori*, the computational cost could be reduced by a factor of

$$\text{Speedup}_{\text{potential}} = \rho^{-1}. \quad (5)$$

In practice, exact identification of \mathcal{S}_ε is not possible without computing the pseudospectra. The central challenge is therefore to design an efficient predictor that identifies \mathcal{S}_ε with high recall while maintaining low computational overhead.

3 Neural Network Approach

In this section, the proposed neural network-based method for accelerating pseudospectra computation is discussed. A classifier is trained that predicts which regions of the complex plane require detailed singular value decomposition. This enables the restriction of expensive computations to a small fraction of the grid while maintaining high coverage of true sensitive zones. We now describe the matrix-level features used to characterize pseudospectral geometry and to condition the neural classifier.

3.1 Matrix Feature Extraction

To enable the neural network to learn geometric properties of pseudospectra from matrix structure alone, we extract a set of size-independent features motivated by classical matrix analysis, conditioning theory, and non-normality measures [21, 2, 1] from input matrix $A \in \mathbb{R}^{n \times n}$.

To extract informative matrix features, we first normalize the input matrix as

$$\tilde{A} = \frac{A}{\|A\|_F + \epsilon},$$

where $\|A\|_F$ denotes the Frobenius norm and $\epsilon \approx 10^{-12}$ ensures numerical stability. This normalization enforces scale invariance, allowing the extracted features to remain comparable across matrices of different magnitudes.

Let $\{\lambda_i\}_{i=1}^n$ and $\{\sigma_i\}_{i=1}^n$ denote the eigenvalues and singular values of A , respectively, with singular values ordered as $\sigma_1 \geq \sigma_2 \geq \dots \geq \sigma_n$. Based on these quantities, we compute a set of 23 global features that capture key spectral, structural, and conditioning properties of the matrix, as summarized in Table 1. These features are designed to provide a compact representation of matrix characteristics that influence the geometry and extent of the pseudospectrum [2, 21].

Given our focus on highly sensitive (non-normal) matrices, the associated eigenvectors are often ill-conditioned, leading to pseudospectra that extend significantly beyond the eigenvalue locations [2]. Consequently, the global matrix features listed in Table 1, while informative, are not sufficient to fully capture the spatial extent and geometry of the pseudospectrum.

To address this limitation, we augment these features with an additional set of seven descriptors (see Tables 2 and 3) specifically designed to quantify spectral spread, non-normality, and resolvent growth. These additional features provide indirect but informative estimates of how far the pseudospectrum extends from the eigenvalues, thereby enabling the model to better predict sensitive regions in the complex plane.

Eigenvector conditioning plays a central role in spectral sensitivity, as characterized by classical perturbation results such as the Bauer-Fike theorem [22].

Here, in Table 3, $z_\delta = \bar{\lambda} + \delta$, where $\bar{\lambda}$ denotes the eigenvalue centroid. The resolvent norm $\|(z_\delta I - A)^{-1}\|$ is estimated by solving

$$(z_\delta I - A)x = b,$$

for a random vector $b \sim \mathcal{N}(0, I)$ and computing the ratio $\|x\|_2 / \|b\|_2$.

These additional features complement global matrix descriptors by capturing spectral sensitivity and resolvent growth effects. In particular, non-normal matrices exhibit pseudospectral regions that can extend far beyond the eigenvalue locations, and this behavior depends on both eigenvector conditioning and resolvent growth [2, 1]. Therefore, augmenting global descriptors with features related to spectral spread and resolvent estimates improves the predictive capability of the model.

The behavior of the pseudospectra is influenced by local geometry of the eigenvalues (Def. 2.1). For each grid point $z = x + iy \in \mathbb{C}$, we compute three per-point eigenvalue distance features:

$$g_1(z) = \min_i |z - \lambda_i|, \quad g_2(z) = |z - \lambda^*|, \quad g_3(z) = \frac{1}{n} \sum_{i=1}^n |z - \lambda_i|. \quad (6)$$

Table 1: Global matrix features extracted from $A \in \mathbb{R}^{n \times n}$, including eigenvalue statistics, spectral spread, non-normality measures, conditioning, matrix norms, and sparsity descriptors. These features provide a compact representation of structural and spectral properties that influence the geometry of the pseudospectrum.

Eigenvalue			
$f_1 = \text{mean}(\Re(\lambda_i))$	$f_2 = \text{std}(\Re(\lambda_i))$	$f_3 = \min_i \Re(\lambda_i)$	$f_4 = \max_i \Re(\lambda_i)$
$f_5 = \text{mean}(\Im(\lambda_i))$	$f_6 = \text{std}(\Im(\lambda_i))$	$f_7 = \min_i \Im(\lambda_i)$	$f_8 = \max_i \Im(\lambda_i)$,
Spectral spread Non-normality measures			
$f_9 = \max_i \lambda_i $	$f_{10} = \min_i \lambda_i $	$f_{11} = \frac{1}{\ A\ _F} \ A - A^T\ _F$	$f_{12} = \frac{1}{\ A\ _F} \ A - A^H\ _F$
Conditioning			
$f_{13} = \log_{10}(\kappa(A) + \epsilon)$, Here, $\kappa(A) = \frac{\sigma_1}{\sigma_n}$, and $\epsilon = 10^{-12}$ ensure numerical stability.			
Matrix norms			
$f_{14} = \frac{1}{\ A\ _F} \ A\ _2$, $f_{15} = \frac{1}{\ A\ _F} \ A\ _1$, $f_{16} = \frac{1}{\ A\ _F} \ A\ _\infty$.			
Diagonal & off-diagonal properties			
$f_{17} = \text{mean}(\text{diag}(A))$	$f_{18} = \text{std}(\text{diag}(A))$	$f_{19} = \text{mean}(A - \text{diag}(\text{diag}(A)))$	$f_{20} = \text{std}(A - \text{diag}(\text{diag}(A)))$
Sparsity & distribution			
$f_{21} = \frac{1}{n^2} \sum_{i,j} \mathbb{I}(A_{ij} > 10^{-10})$, $f_{22} = \text{mean}(\tilde{A}^2)$, $f_{23} = \text{std}(\tilde{A}^2)$.			

Table 2: Additional matrix features designed to capture spectral sensitivity and non-normality effects. These include eigenvector conditioning, logarithmic non-normality ratios, and measures of singular value and eigenvalue spread, which are critical for estimating pseudospectral expansion beyond eigenvalue locations.

eigenvector condition number & logarithmic non-normality ratio
$f_{24} = \log_{10}(\kappa(V) + \delta)$, $f_{25} = \log_{10}\left(\frac{\ A - A^H\ _F}{\ A\ _F} + \epsilon\right)$.
Singular value & Eigenvalue spread
$f_{26} = \frac{\sigma_1 - \sigma_n}{\sigma_1 + \epsilon}$, $f_{27} = \frac{\max_i \lambda_i - \min_i \lambda_i }{\max_i \lambda_i + \epsilon}$

These distance-based features provide local geometric context relative to the spectrum, enabling the network to adapt its predictions based on proximity to eigenvalues in the complex plane.

$$\mathbf{f}(z, A) = [f_1, f_2, f_3, \dots, f_{29}, f_{30}, g_1(z), g_2(z), g_3(z)] \in \mathbb{R}^{33}. \quad (7)$$

Table 3: Resolvent-based features computed at shifted points $z_\delta = \bar{\lambda} + \delta$ for $\delta \in \{0.5, 1.0, 2.0\}$, where $\bar{\lambda}$ denotes the eigenvalue centroid. These quantities approximate resolvent norm growth and provide insight into pseudospectral sensitivity away from the spectrum.

Resolvent norm $\ (z_\delta I - A)^{-1}\ $ at distinct $\delta = 0.5, 1.0, 2.0$		
$f_{28} = \log_{10}(\ (z_{0.5} I - A)^{-1}\)$	$f_{29} = \log_{10}(\ (z_{1.0} I - A)^{-1}\)$	$f_{30} = \log_{10}(\ (z_{2.0} I - A)^{-1}\)$

These features are incorporated into the neural network architecture as described in the next subsection.

3.2 Network Architecture

In our approach, the classifier consists of two parallel pathways that process spatial coordinates and matrix features separately before fusion. We first describe the encoding used for spatial coordinates in the complex plane.

3.2.1 Fourier Feature Encoding

Grid coordinates $z = x + iy$ are first encoded using Fourier features to capture periodic structure arising from oscillatory level sets of the resolvent norm in the complex plane. The number of frequency bands is chosen to balance expressive power with computational efficiency, providing sufficient resolution to capture fine-scale pseudospectral structure without over-parameterization. For coordinate input $\mathbf{c} = [x, y]^T \in \mathbb{R}^2$, we compute

$$\phi(\mathbf{c}) = [\mathbf{c}, \sin(2\mathbf{c}), \cos(2\mathbf{c}), \sin(4\mathbf{c}), \cos(4\mathbf{c}), \dots, \sin(2^6\mathbf{c}), \cos(2^6\mathbf{c})]^T \quad (8)$$

where the maximum frequency is $2^6 = 64$, the sine and cosine functions are applied element-wise across six frequency bands ($2^1, 2^2, \dots, 2^6$), yielding a compact multi-scale representation of the spatial coordinates [23].

The encoded spatial coordinates are then combined with matrix-dependent features within a dual-path network architecture, which we describe next.

3.2.2 Dual-Path Architecture

The Fourier-encoded coordinates are mapped through two fully-connected layers

$$\mathbf{h}_c^{(1)} = \text{SiLU}(W_c^{(1)}\phi(\mathbf{c}) + b_c^{(1)}), \quad W_c^{(1)} \in \mathbb{R}^{64 \times 26}, \quad (9)$$

$$\mathbf{h}_c^{(2)} = \text{SiLU}(W_c^{(2)}\mathbf{h}_c^{(1)} + b_c^{(2)}), \quad W_c^{(2)} \in \mathbb{R}^{64 \times 64}. \quad (10)$$

The 33-dimensional feature vector $\mathbf{f}(z, A)$ is mapped through

$$\mathbf{h}_m^{(1)} = \text{SiLU}(W_m^{(1)}\mathbf{f}(z, A) + b_m^{(1)}), \quad W_m^{(1)} \in \mathbb{R}^{128 \times 33}, \quad (11)$$

$$\mathbf{h}_m^{(2)} = \text{SiLU}(W_m^{(2)}\mathbf{h}_m^{(1)} + b_m^{(2)}), \quad W_m^{(2)} \in \mathbb{R}^{64 \times 128}. \quad (12)$$

The two pathways are subsequently concatenated

$$\mathbf{h}^{(3)} = [\mathbf{h}_c^{(2)}, \mathbf{h}_m^{(2)}] \in \mathbb{R}^{128}. \quad (13)$$

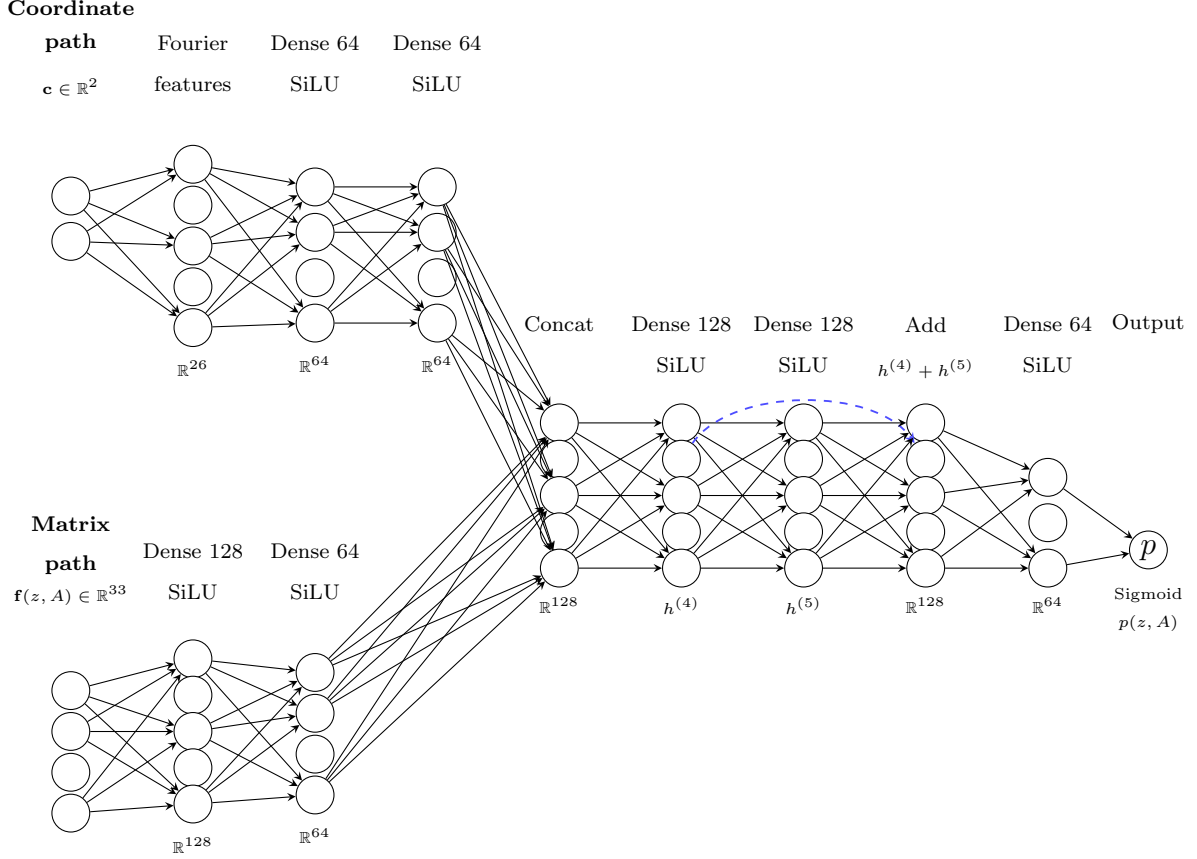


Figure 4: Neural network architecture for pseudospectra prediction. The coordinate pathway (top) processes spatial locations via Fourier features, while the matrix pathway (bottom) processes 33 combined features (30 global matrix properties + 3 per-point eigenvalue distances). Both pathways converge at the central concatenation layer. After concatenation, a residual block (with skip connection in blue) refines the representation before sigmoid output $p(z, A) = P(\text{sensitive} \mid z, A)$.

This fused representation is processed through a residual block [24] to enhance representational capacity while stabilizing optimization.

$$\mathbf{h}^{(4)} = \text{SiLU} (W^{(4)}\mathbf{h}^{(3)} + b^{(4)}), \quad W^{(4)} \in \mathbb{R}^{128 \times 128}, \quad (14)$$

$$\mathbf{h}^{(5)} = \text{SiLU} (W^{(5)}\mathbf{h}^{(4)} + b^{(5)}), \quad W^{(5)} \in \mathbb{R}^{128 \times 128}, \quad (15)$$

$$(16)$$

The residual connection is then applied as

$$\mathbf{h}^{(6)} = \mathbf{h}^{(4)} + \mathbf{h}^{(5)} \quad (17)$$

The representation is then projected to a lower dimension

$$\mathbf{h}^{(7)} = \text{SiLU} (W^{(7)}\mathbf{h}^{(6)} + b^{(7)}), \quad W^{(7)} \in \mathbb{R}^{64 \times 128}. \quad (18)$$

Finally, a sigmoid layer produces the probability that point z lies within the ε -pseudospectrum:

$$p(z, A; \theta) = \sigma (w^T \mathbf{h}^{(7)} + b), \quad (19)$$

where $\sigma(x) = \frac{1}{1+e^{-x}}$ is the sigmoid function, $w \in \mathbb{R}^{64}$, and θ denotes all trainable parameters.

We use the SiLU (Swish) activation function [25] $\text{SiLU}(x) = x \cdot \sigma(x)$ throughout the network, which provides smooth, non-monotonic gradients that facilitate optimization. The network contains approximately 45,000 trainable parameters, making it lightweight enough for rapid inference while remaining sufficiently expressive to capture complex pseudospectral geometries. Having described the network architecture, we now detail the procedure used to construct the training data.

3.3 Training Data Generation

The training data are generated using random banded non-normal matrices, which provide a computationally efficient yet sufficiently rich class of matrices exhibiting nontrivial pseudospectral behavior. For each matrix $A \in \mathbb{R}^{64 \times 64}$, the bandwidth $\beta \in \{1, 2, 3, 4\}$ is sampled uniformly, and the matrix entries are defined as

$$A_{ij} = \begin{cases} \text{uniform}\{-1, 0, 1\}, & \text{if } |i - j| \leq \beta, \\ 0, & \text{otherwise.} \end{cases} \quad (20)$$

We additionally enforce $A \neq A^T$ to ensure non-normality and restrict the condition number to $\kappa(A) < 10^8$ to avoid extreme numerical instability.

For each matrix, ground-truth pseudospectra are computed on a 100×100 grid over the domain $[-4, 4] \times [-4, 4]$ in the complex plane with threshold $\varepsilon = 0.01$, which provides a suitable resolution for capturing relevant spectral sensitivity.

A grid point z is labeled as sensitive if $\sigma_{\min}(zI - A) \leq \varepsilon$.

To address the inherent class imbalance between sensitive and non-sensitive grid points, we adopt the following sampling strategy.

3.3.1 Balanced Sampling Strategy

Direct grid sampling produces severe class imbalance, with typically fewer than 5% of grid points classified as sensitive. To address this issue, we adopt a targeted sampling strategy that partitions the data into two classes [26, 27]. For each matrix, all sensitive grid points are included in the positive class. For the negative class, we randomly sample $\max(10 n_{\text{pos}}, 200)$ non-sensitive points, where n_{pos} denotes the number of sensitive points for that matrix.

This strategy ensures sufficient representation of the positive class while maintaining a manageable dataset size. Using 500 training matrices, this procedure yields a total of 438,084 labeled samples. The resulting dataset is then used to optimize the network parameters as described below.

3.4 Loss Function and Optimization

We train the neural network using binary cross-entropy [10]

$$\mathcal{L}(\theta) = -\frac{1}{N} \sum_{i=1}^N [y_i \log p_i + (1 - y_i) \log(1 - p_i)], \quad (21)$$

where $y_i \in \{0, 1\}$ denotes the ground-truth label and $p_i = p(z_i, A_i; \theta)$ is the predicted probability. Optimization is performed using the Adam optimizer [28] with a learning rate

of 10^{-3} and batch size 512. The network is trained for up to 25 epochs with early stopping based on validation loss, using a patience of 5 epochs.

During inference, evaluating the classifier efficiently over the complex plane becomes critical.

3.5 Hierarchical Prediction Strategy

Direct evaluation of the network on a 100×100 grid requires 10,000 forward passes. We mitigate this cost using a hierarchical coarse-to-fine prediction strategy [29]. We first evaluate the network on a coarse 25×25 grid, corresponding to every fourth grid point. Let P_{coarse} denote the resulting predicted probability map. Candidate regions are identified using an 80th-percentile threshold

$$\tau_{\text{coarse}} = \text{quantile}_{0.8}(P_{\text{coarse}}). \quad (22)$$

For each coarse grid cell $[i : i + 4, j : j + 4]$ satisfying $P_{\text{coarse}}[i, j] \geq \tau_{\text{coarse}}$, the network is evaluated on all $4 \times 4 = 16$ fine-grid points within that cell. Cells below the threshold are assigned zero probability. This hierarchical procedure reduces the number of network evaluations from 10,000 to approximately $625 + 0.2(10,000 - 625) \approx 2,625$ on average, with minimal impact on prediction accuracy. To convert predicted probabilities into a binary sensitive region, an appropriate decision threshold is required.

3.6 Threshold Calibration

The raw network probabilities must be converted into binary predictions. To this end, we calibrate the classification threshold τ on a held-out validation set of 30 matrices, with the objective of maximizing recall while controlling false positives. For each candidate threshold $\tau \in \{0.05, 0.06, \dots, 0.94\}$, the network predictions $\hat{S} = \{z : p(z, A) \geq \tau\}$ are first post-processed using morphological dilation with a 5×5 structuring element [30, 31] to provide a safety margin. Recall is then computed against the ground-truth sensitive regions, which are themselves dilated using a 3×3 structuring element to account for minor spatial misalignments. The final threshold is selected according to

$$\tau^* = \min \{ \tau : \text{median}_{\text{val}}(\text{recall}) \geq 0.90 \text{ and } P_{10}(\text{recall}) \geq 0.75 \}, \quad (23)$$

where P_{10} denotes the 10th percentile across the validation set. This criterion enforces both strong typical performance and robustness in worst-case scenarios. On the validation set, we obtain $\tau^* = 0.05$, yielding a median recall of 1.000 and a 10th-percentile recall of 1.000.

In practice, the proposed method integrates neural network guidance with selective singular value computations in a coarse-to-fine framework. The network is first used to localize a small subset of grid points likely to belong to the ε -pseudospectrum, after which exact singular value decompositions are performed only within this predicted region. The final pseudospectrum is then constructed by thresholding $\sigma_{\min}(zI - A)$ on the restricted grid, while all remaining points are classified as non-sensitive.

From a computational standpoint, the dominant cost arises from the singular value decompositions. Network inference scales linearly with the number of evaluated grid points and is carried out on a coarse grid followed by refinement on only a limited fraction of fine-grid locations. This results in $O(N_{\text{coarse}} + f N_{\text{fine}})$ network evaluations, where $f \approx 0.26$ denotes the fraction of fine-grid points selected for refinement. Exact singular value computations are subsequently restricted to the predicted region, leading to a cost proportional to $O(|x_{\text{in}}| |y_{\text{in}}| n^3)$, with $|x_{\text{in}}| |y_{\text{in}}| \approx 0.16 N_x N_y$ in our experiments. As a result, evaluating

only a small portion of the grid yields substantial computational savings compared to full pseudospectrum computation.

The above analysis clarifies how restricting singular value decompositions to a carefully selected subset of the complex plane can substantially reduce computational cost without compromising accuracy. We now formalize this idea by presenting a hybrid computational framework that integrates neural network prediction with exact numerical evaluation. The goal is to translate the learned localization capability into a principled algorithmic strategy with transparent computational complexity.

4 Hybrid Computational Approach

Having established the mathematical foundations in Sec. 2 and detailed the neural network architecture in Sec. 3, we now describe the complete hybrid computational strategy. Given a matrix $A \in \mathbb{C}^{n \times n}$ and a computational grid \mathcal{G} defined over a rectangular domain in the complex plane, our approach computes an approximation $\tilde{\mathcal{S}}_\varepsilon$ to the sensitive zone \mathcal{S}_ε through a two-stage process.

First, a trained classifier $f_\theta : \mathbb{C} \times \mathbb{R}^{n \times n} \rightarrow [0, 1]$ identifies a candidate region $\mathcal{R} \subseteq \mathcal{G}$ that likely contains \mathcal{S}_ε , with $|\mathcal{R}| \ll N$ to achieve computational savings. The classifier is designed to satisfy

$$\mathbb{P}[\mathcal{S}_\varepsilon \subseteq \mathcal{R}] \geq 0.90,$$

through threshold calibration on validation data, where \mathbb{P} denotes probability with respect to the distribution of matrices and grid points used during validation.

Second, exact singular value decompositions are computed only for points $z \in \mathcal{R}$, yielding $\sigma_{\min}(z) = \sigma_{\min}(zI - A)$ to machine precision. The approximate sensitive zone is then defined as

$$\tilde{\mathcal{S}}_\varepsilon = \{z \in \mathcal{R} : \sigma_{\min}(z) \leq \varepsilon\}.$$

This two-stage procedure yields the hybrid computational cost

$$\mathcal{C}_{\text{hybrid}} = \mathcal{C}_{\text{NN}}(N) + |\mathcal{R}| \cdot \mathcal{C}_{\text{SVD}}(n), \quad (24)$$

where $\mathcal{C}_{\text{NN}}(N) = O(N)$ represents the cost of neural network inference over the grid and $\mathcal{C}_{\text{SVD}}(n) = O(n^3)$ is the cost of a single SVD.

Since neural network evaluation is substantially cheaper than SVD—typically $\mathcal{C}_{\text{NN}}(N) \approx 10^{-4} \cdot N \cdot \mathcal{C}_{\text{SVD}}(n)$ for moderate n —and the predicted region satisfies $|\mathcal{R}| \ll N$ by construction, equation (24) represents a significant reduction compared to the full cost $\mathcal{C}_{\text{full}} = N \cdot \mathcal{C}_{\text{SVD}}(n)$ from equation (4).

The theoretical speedup is approximately

$$\text{Speedup}_{\text{theory}} \approx \frac{\mathcal{C}_{\text{full}}}{\mathcal{C}_{\text{hybrid}}} \approx \frac{N}{|\mathcal{R}|} = \rho^{-1}, \quad (25)$$

where $\rho = |\mathcal{R}|/N$ denotes the fraction of the grid requiring SVD computation. In our experiments with banded non-normal matrices, we observe $\rho \approx 0.16$, suggesting potential speedups of approximately $6\times$.

To minimize the cost of neural network evaluations themselves, we employ a hierarchical coarse-to-fine prediction strategy. Rather than evaluating f_θ at all N grid points, we first

construct a coarse grid $\mathcal{G}_{\text{coarse}}$ by subsampling \mathcal{G} with stride $s = 4$ in both spatial dimensions, yielding $N_{\text{coarse}} = N/s^2$ points. The classifier is evaluated on $\mathcal{G}_{\text{coarse}}$, and high-probability regions are identified via adaptive thresholding: $\mathcal{R}_{\text{coarse}} = \{z \in \mathcal{G}_{\text{coarse}} : p(z) \geq \tau_{\text{coarse}}\}$, where τ_{coarse} is defined as the 80th percentile of coarse-grid predictions $\{p(z) : z \in \mathcal{G}_{\text{coarse}}\}$. This percentile-based threshold adapts to the specific pseudospectral structure of each matrix.

All fine-grid points lying within cells flagged by $\mathcal{R}_{\text{coarse}}$ are then collected into a refinement region $\mathcal{R}_{\text{fine}}$, and the classifier is evaluated on this subset. A calibrated decision threshold τ —determined independently via the validation procedure described in Section 3—is applied to obtain the final predicted region $\mathcal{R} = \{z \in \mathcal{R}_{\text{fine}} : p(z) \geq \tau\}$. To ensure robustness near pseudospectral boundaries and account for discretization effects, \mathcal{R} is expanded using a 5×5 morphological dilation. This hierarchical scheme reduces the total number of network evaluations from N to approximately $N/16 + |\mathcal{R}_{\text{fine}}| \approx 2,625$ for a 100×100 grid, where typically $|\mathcal{R}_{\text{fine}}| \approx 0.2N$.

4.1 Complexity Analysis

The total computational cost decomposes as

$$\mathcal{C}_{\text{hybrid}} = \underbrace{O(n^3)}_{\text{eigenvalues}} + \underbrace{O(N/s^2)}_{\text{coarse NN}} + \underbrace{O(|\mathcal{R}_{\text{fine}}|)}_{\text{fine NN}} + \underbrace{|\mathcal{R}| \cdot O(n^3)}_{\text{restricted SVD}}. \quad (26)$$

For typical problem sizes ($n = 64$, $N = 10^4$, $|\mathcal{R}| \approx 0.16N$), the dominant term is the restricted SVD stage. The actual speedup realized in practice is

$$\text{Speedup}_{\text{actual}} = \frac{t_{\text{full}}}{t_{\text{NN}} + t_{\text{restricted SVD}}}, \quad (27)$$

where timing measurements account for implementation overhead. As shown in Section 5, we observe speedups of $2.45\times$ on average, with the discrepancy from theoretical speedup (25) arising from neural network inference time and conservative region padding.

4.2 Error Characteristics

The proposed hybrid strategy admits only a limited and well-controlled form of approximation error. If $\mathcal{S}_\epsilon \not\subseteq \mathcal{R}$, some truly sensitive points are omitted. This is controlled via threshold calibration targeting $\geq 90\%$ recall on validation data. Critically, the method computes *exact* $\sigma_{\min}(z)$ for all $z \in \mathcal{R}$ via SVD. Thus, within the predicted region, all values are correct to machine precision. Errors manifest only as omissions, not incorrect predictions.

This error structure is favorable for applications where conservative estimates are acceptable, provided that computed values are reliable where available. We now empirically assess the effectiveness of this approach in terms of both accuracy and computational efficiency through a series of numerical experiments.

5 Numerical Experiments

We evaluate the proposed hybrid pseudospectra computation method on randomly generated banded non-normal matrices and compare its performance against both exhaustive grid evaluation and a random sampling baseline.

5.1 Experimental Setup

Test matrices are generated from the same class of random banded non-normal matrices defined in (20), with matrix size $A \in \mathbb{R}^{64 \times 64}$ and bandwidth $\beta \in \{1, 2, 3, 4\}$ sampled uniformly. This ensures that the test problems share the same structural characteristics as the training data while remaining disjoint from the training and validation sets. The neural network is trained using the procedure described in Sec. 3 and is kept fixed for all experiments reported in this section. Threshold calibration is performed on a separate validation set of 30 matrices, yielding a calibrated decision threshold $\tau^* = 0.05$, which is used consistently throughout all numerical experiments.

Using this trained model and calibrated threshold, we evaluate the performance on 50 held-out test matrices generated from the same distribution as the training data but disjoint from both the training and validation sets. For each test matrix, the ground-truth ε -pseudospectrum is computed using full singular value decomposition on a 100×100 grid over $[-4, 4] \times [-4, 4]$ in the complex plane with $\varepsilon = 0.01$. The proposed hybrid method combines neural network predictions with restricted singular value decompositions in a coarse-to-fine manner, as described in the preceding section. For comparison, we also consider a random sampling baseline that evaluates an identical fraction of grid points selected uniformly at random. All timing measurements are performed using a single CPU thread in order to exclude any effects of parallelization or hardware acceleration. The accuracy and efficiency of these evaluations are quantified using the performance metrics described below.

5.2 Performance Metrics

We assess the proposed method using both classification accuracy measures and computational efficiency indicators. To account for boundary uncertainty in the pseudospectrum, the ground-truth sensitive region is dilated using a 3×3 structuring element prior to metric computation. Let $S_{\text{true}}^{\text{dilated}}$ denote the dilated ground-truth region and S_{true} the original sensitive region.

Classification performance is quantified by accuracy, precision, recall, and coverage. Accuracy measures the fraction of correctly classified grid points. Precision is defined as

$$\frac{|S_{\text{true}} \cap S_{\text{pred}}|}{|S_{\text{pred}}|},$$

reflecting the purity of the predicted sensitive region.

Recall is defined as

$$\frac{|S_{\text{true}}^{\text{dilated}} \cap S_{\text{pred}}|}{|S_{\text{true}}^{\text{dilated}}|},$$

which measures the fraction of true sensitive points successfully identified. Recall is computed with respect to the dilated ground-truth region, while coverage is evaluated on the original sensitive region, providing a complementary measure of prediction completeness.

Coverage is defined as the fraction of true sensitive points captured by the predicted region, i.e.,

$$\frac{|S_{\text{true}} \cap S_{\text{pred}}|}{|S_{\text{true}}|}.$$

Computational efficiency is evaluated by measuring the fraction of grid points on which singular value decompositions are performed, referred to as the grid fraction. We further report

Table 4: Performance statistics over 50 test matrices (mean \pm std).

Metric	Mean	Std	Median	Range
<i>Classification Performance</i>				
Accuracy	0.869	0.024	0.870	[0.815, 0.927]
Precision	0.175	0.059	0.173	[0.058, 0.284]
Recall	0.995	0.014	1.000	[0.922, 1.000]
Coverage	0.998	0.007	1.000	[0.964, 1.000]
<i>Computational Efficiency</i>				
Grid fraction	0.159	0.032	0.166	[0.090, 0.219]
Speedup (actual)	2.45	0.36	2.50	[1.50, 3.09]
Speedup (best-case)	3.52	0.91	3.34	[1.77, 5.84]
<i>Timing (seconds)</i>				
Full SVD	3.73	0.99	4.14	[1.73, 4.85]
NN prediction	0.38	0.07	0.36	[0.31, 0.66]
Restricted SVD	1.19	0.52	1.32	[0.32, 2.39]
Hybrid total	1.57	0.53	1.65	[0.64, 2.82]

the actual speedup, defined as $\frac{t_{\text{full}}}{(t_{\text{NN}}+t_{\text{restricted}})}$, which accounts for both neural network inference and restricted singular value computations, as well as the best-case speedup, $\frac{t_{\text{full}}}{t_{\text{restricted}}}$, which excludes neural network overhead and represents an upper bound on achievable acceleration.

Having defined the evaluation criteria, we now summarize the empirical performance of the proposed hybrid method across a collection of unseen test matrices. The following results quantify the trade-off between accuracy and computational efficiency achieved by restricting expensive singular value computations to network-predicted regions of interest.

5.3 Main Results

Table 4 summarizes performance across 50 test matrices. The method achieves high recall (99.5% \pm 1.4%) and coverage (99.8% \pm 0.7%) while evaluating only 15.9% \pm 3.2% of grid points, resulting in 2.45 \times average speedup over exhaustive evaluation.

The low precision (17.5%) reflects conservative prediction: the network identifies approximately 16% of the grid as potentially sensitive, while ground truth typically contains < 1% sensitive points (mean 83 points out of 10,000). However, high recall and coverage confirm that nearly all true sensitive points are captured within predicted regions.

Figure 5 illustrates representative examples showing ground truth pseudospectra alongside neural network predictions. The network successfully identifies sensitive regions of varying shapes and extents across different matrix structures. Figure 6 shows classification metrics and speedup remain consistently high across all 50 test matrices, with the hybrid method achieving faster computation than full SVD in every trial.

To further examine how structural properties of the matrix influence performance, we next analyze the results as a function of matrix bandwidth, which directly controls sparsity and the complexity of the resulting pseudospectra.

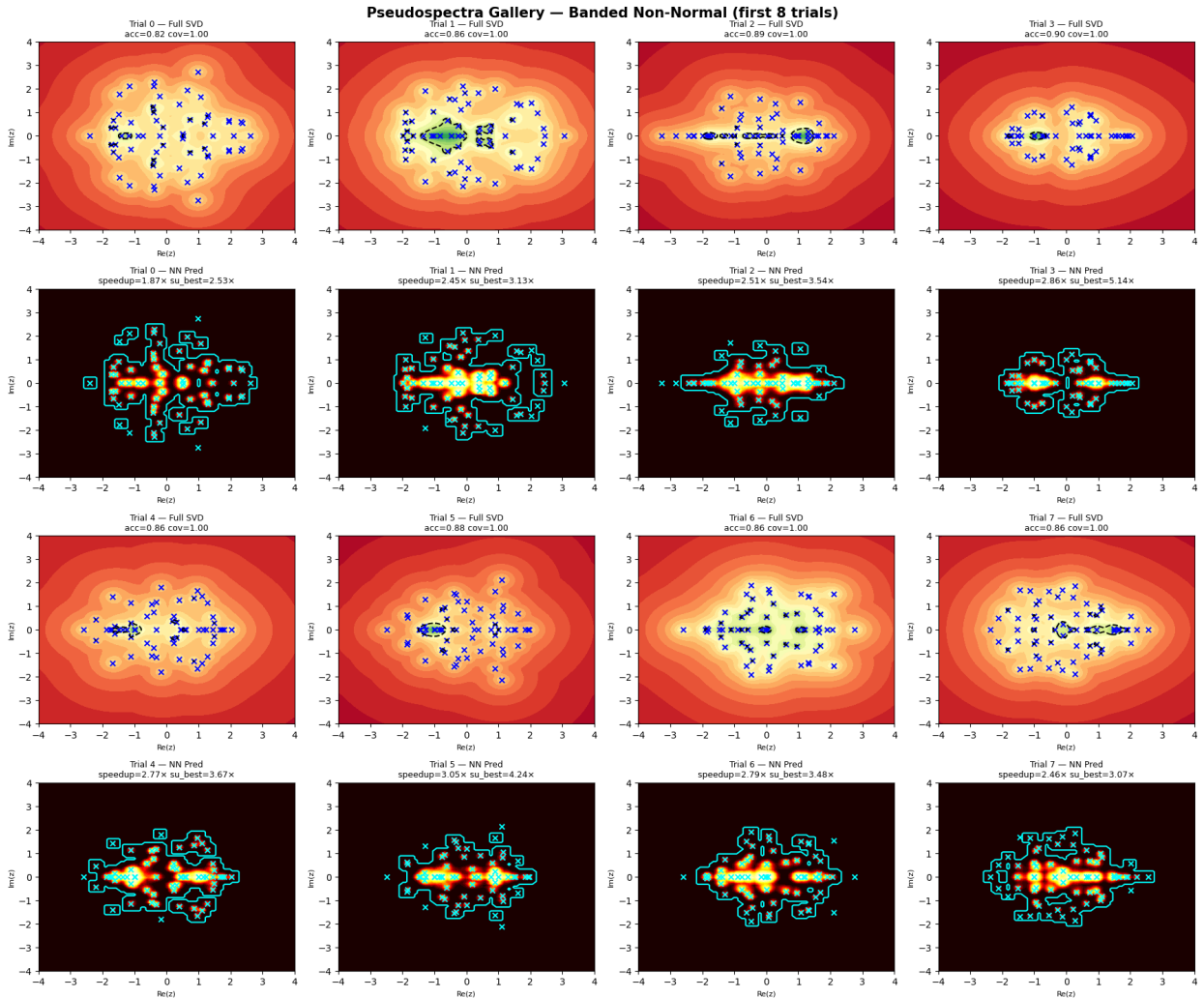


Figure 5: Pseudospectra comparison on eight representative test matrices. For each matrix, top panel shows ground truth $\log(\sigma_{\min}(zI - A))$ with ε -pseudospectra boundary (black contour) and eigenvalues (blue crosses). Bottom panel shows neural network probability map with predicted sensitive region (cyan contour) and eigenvalues (cyan crosses). The method accurately captures diverse pseudospectra geometries across bandwidth values $\beta \in \{1, 2, 3, 4\}$.

5.4 Bandwidth Stratification

Table 5 stratifies results by matrix bandwidth. Performance degrades slightly for larger bandwidth: matrices with $\beta = 1$ achieve $2.56\times$ speedup with perfect recall, while $\beta = 2$ achieves $2.70\times$ speedup. For larger bandwidth values, performance gradually degrades: $\beta = 4$ yields $2.06\times$ speedup with 98.4% recall. This occurs because larger bandwidth produces more complex pseudospectra with broader sensitive regions, reducing the benefit of domain restriction.

Despite this variation, the method maintains $> 98\%$ recall across all bandwidth values, demonstrating robustness to structural diversity within the banded matrix class. To further contextualize these results, we compare the proposed method with a random sampling baseline that evaluates the same fraction of grid points but without exploiting geometric information.

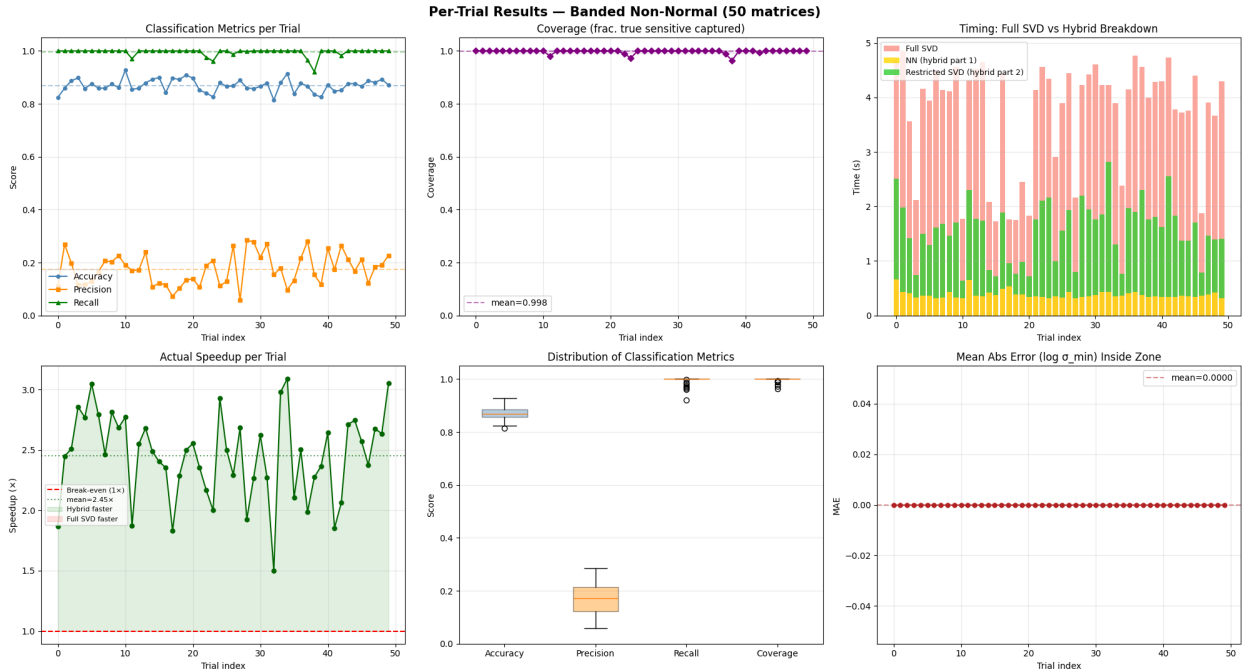


Figure 6: Performance metrics across 50 test matrices. (a) Classification metrics per trial: accuracy (blue circles), precision (orange squares), and recall (green triangles) with mean values shown as dashed lines. (b) Coverage per trial (purple diamonds) showing fraction of true sensitive points captured. (c) Timing breakdown: full SVD (salmon), neural network overhead (gold), and restricted SVD (green). (d) Speedup per trial showing all matrices achieve $> 1.5\times$ acceleration. (e) Distribution of classification metrics. (f) Mean absolute error in $\log(\sigma_{\min})$ within predicted zones.

Table 5: Performance stratified by bandwidth (mean \pm std).

Bandwidth	Count	Speedup	Recall (%)	Coverage (%)
$\beta = 1$	12	2.56 ± 0.32	100.0 ± 0.0	100.0 ± 0.0
$\beta = 2$	11	2.70 ± 0.20	100.0 ± 0.0	100.0 ± 0.0
$\beta = 3$	15	2.50 ± 0.28	99.7 ± 0.8	99.9 ± 0.5
$\beta = 4$	12	2.06 ± 0.25	98.4 ± 2.3	99.3 ± 1.1

5.5 Comparison with Random Sampling

To isolate the value of geometric guidance, we compare against a random sampling baseline that evaluates the same fraction of grid points (15.9%) but selects them uniformly at random rather than using neural network predictions.

Table 6 shows that random sampling achieves only $45.9\% \pm 14.2\%$ recall compared to our method’s $99.5\% \pm 1.4\%$ recall. The high standard deviation (14.2%) in random sampling indicates unreliable performance: some matrices yield acceptable coverage by chance, while others miss most sensitive points entirely.

Figure 7 compares the distributions of recall, precision, and coverage between random sampling and our method. The dramatic improvement in recall consistency (1.4% vs 14.2% standard deviation) demonstrates that learned geometric structure drives reliable performance.

Table 6: Method comparison (mean \pm std over 50 matrices).

Method	Coverage (%)	Recall (%)	Precision (%)	Speedup
Full SVD	100.0	100.0	–	1.00 \times
Random sampling	15.9 \pm 3.2	45.9 \pm 14.2	66.7 \pm 10.9	6.28 \times (theor.)
Hybrid (ours)	15.9 \pm 3.2	99.5 \pm 1.4	17.5 \pm 5.9	2.45 \times (actual)

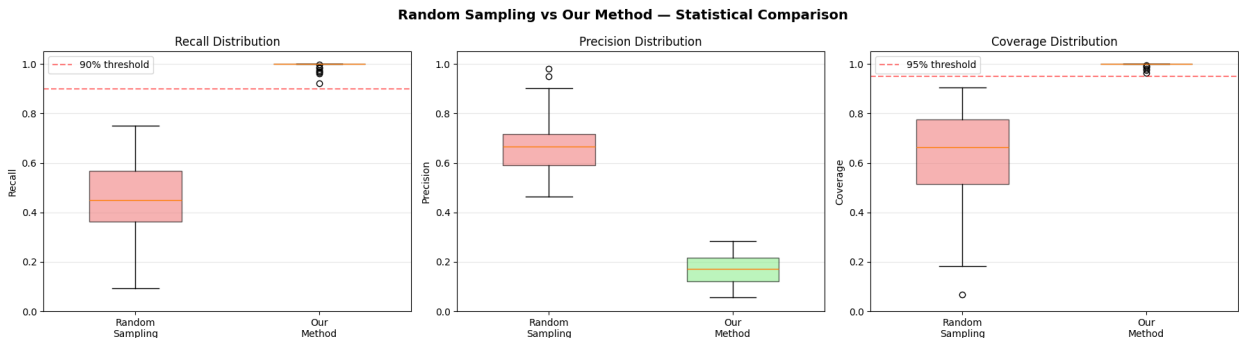


Figure 7: Comparison with random sampling baseline over 50 test matrices. Box plots show (a) recall, (b) precision, and (c) coverage distributions. Random sampling (red) exhibits high variance and poor median recall (45.9%), while our method (green) achieves consistent high recall (99.5%) with low variance. Red dashed lines indicate target thresholds.

The theoretical speedup for random sampling (6.28 \times) assumes zero overhead, while our actual speedup (2.45 \times) includes neural network evaluation time (0.38s average). However, random sampling’s poor recall renders the theoretical speedup meaningless: a method that misses half the sensitive points cannot reliably compute pseudospectra.

Our method achieves 39.1% efficiency relative to the theoretical maximum ($2.45/6.28 = 0.391$), trading some speed for substantially improved reliability. The +53.6 percentage point gain in recall over random sampling demonstrates that accuracy is driven by learned geometric structure rather than mere reduction in computational budget. We now examine the computational efficiency of the proposed approach by analyzing its runtime characteristics and resulting speedup behavior.

5.6 Timing Analysis

Figure 8 breaks down timing components and speedup distributions. The neural network overhead (0.38s average) is modest relative to the time saved by restricted evaluation: full SVD requires 3.73s average, while our hybrid approach requires 1.57s average.

The difference between the observed speedup (2.45 \times) and the best-case speedup (3.52 \times) is attributable to the overhead introduced by neural network inference. As matrix dimension increases and the cost of singular value decomposition scales as $O(n^3)$, this overhead becomes progressively less significant, indicating the potential for greater acceleration at larger problem sizes. Network evaluation itself scales sublinearly with grid size due to the hierarchical prediction strategy: the coarse stage requires only 625 evaluations, and refinement is performed on approximately 26% of the fine grid, resulting in an average of 2,625 network evaluations compared to 10,000 for full-grid evaluation. This hierarchical design substantially reduces inference overhead while preserving prediction accuracy.

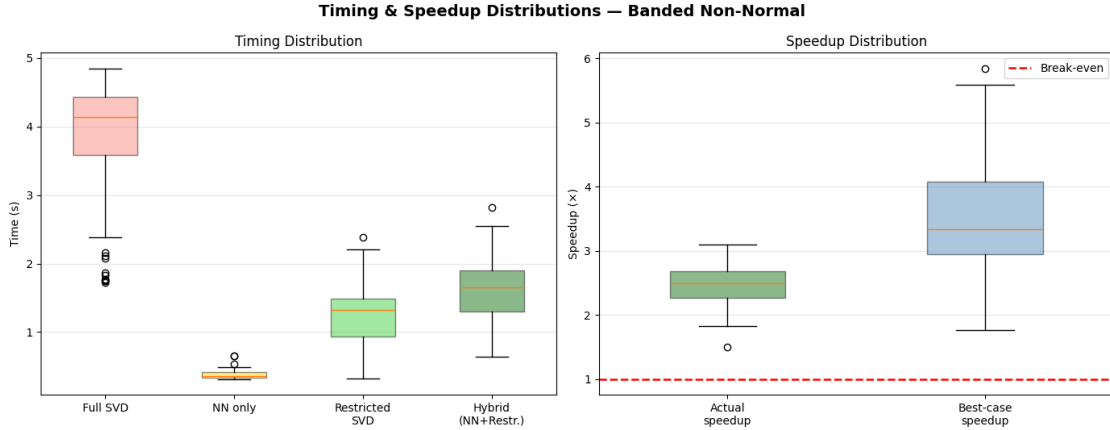


Figure 8: Timing and speedup distributions over 50 test matrices. Left panel: absolute timing for full SVD (red), neural network only (yellow), restricted SVD (green), and total hybrid method (dark green). Right panel: actual speedup (green) and best-case speedup excluding network overhead (blue), with break-even line at $1\times$ (red dashed).

6 Discussion

The effectiveness of the proposed hybrid framework arises from the combination of three key components: geometry-aware feature design, conservative threshold calibration, and hierarchical prediction. Together, these elements enable reliable identification of pseudospectrally sensitive regions while significantly reducing the number of singular value decompositions.

The feature representation integrates global matrix descriptors with local eigenvalue distance information, allowing the model to capture both overall pseudospectral behavior and spatial variation. In addition, features related to eigenvector conditioning and resolvent estimates provide indicators of spectral sensitivity beyond eigenvalue location alone.

The method is intentionally conservative: threshold calibration and morphological dilation prioritize high recall, ensuring that sensitive regions are not missed. This design reflects the asymmetric cost of errors, where false negatives are significantly more harmful than false positives.

The hierarchical coarse-to-fine strategy further improves efficiency by restricting both neural network evaluation and SVD computations to candidate regions, reducing overhead without sacrificing accuracy.

A limitation of the current study is its focus on banded non-normal matrices. While the framework is general, its performance on other matrix classes remains to be investigated. Moreover, training requires labeled pseudospectra, which introduces an upfront computational cost.

Overall, the results demonstrate that learned geometric structure can effectively guide numerical computation, enabling substantial acceleration while maintaining reliability.

7 Conclusion

We presented a neural-guided hybrid framework for accelerating pseudospectra computation of non-normal matrices. By predicting spectrally sensitive regions using matrix features, the

method restricts expensive singular value decompositions to a small subset of the complex plane.

Experiments on banded non-normal matrices show that the approach evaluates only about 16% of grid points while achieving approximately $2.45\times$ speedup and maintaining high reliability, with 99.5% recall and 99.8% coverage.

The results demonstrate that data-driven domain restriction can effectively complement classical numerical methods, providing a practical strategy for efficient pseudospectra computation. Future work includes extending the approach to broader matrix classes and evaluating performance at larger problem scales.

References

- [1] Lloyd N. Trefethen. Pseudospectra of linear operators. *SIAM Review*, 39(3):383–406, 1997.
- [2] Lloyd N. Trefethen and Mark Embree. *Spectra and Pseudospectra: The Behavior of Nonnormal Matrices and Operators*. Princeton University Press, Princeton, NJ, 2005.
- [3] Lloyd N. Trefethen, Anne E. Trefethen, Satish C. Reddy, and Tobin A. Driscoll. Hydrodynamic stability without eigenvalues. *Science*, 261(5121):578–584, 1993.
- [4] Peter J. Schmid and Dan S. Henningson. *Stability and Transition in Shear Flows*, volume 142 of *Applied Mathematical Sciences*. Springer, New York, 2001.
- [5] Peter J. Schmid. Nonmodal stability theory. *Annual Review of Fluid Mechanics*, 39(Volume 39, 2007):129–162, 2007.
- [6] Mark Embree. How descriptive are gmres convergence bounds? Technical report, Oxford University Computing Laboratory, 1999.
- [7] Lloyd N. Trefethen. Finite difference and spectral methods for ordinary and partial differential equations, 1996. Unpublished text, available at <https://people.maths.ox.ac.uk/trefethen/pdetext.html>.
- [8] Ernst Hairer and Gerhard Wanner. *Solving Ordinary Differential Equations II: Stiff and Differential-Algebraic Problems*, volume 14 of *Springer Series in Computational Mathematics*. Springer, Berlin, 1996.
- [9] Stefan Rotter and Sylvain Gigan. Light fields in complex media: Mesoscopic scattering meets wave control. *Reviews of Modern Physics*, 89:015005, Mar 2017.
- [10] Ian Goodfellow, Yoshua Bengio, and Aaron Courville. *Deep Learning*. MIT Press, Cambridge, MA, 2016.
- [11] George E. Karniadakis, Ioannis G. Kevrekidis, Lu Lu, Paris Perdikaris, Sifan Wang, and Liu Yang. Physics-informed machine learning. *Nature Reviews Physics*, 3(6):422–440, 2021.
- [12] Lu Lu, Pengzhan Jin, Guofei Pang, Zhongqiang Zhang, and George E. Karniadakis. Learning nonlinear operators via deeponet based on the universal approximation theorem of operators. *Nature Machine Intelligence*, 3(3):218–229, 2021.

- [13] A. Zettl. *Sturm-Liouville Theory*. Mathematical surveys and monographs. American Mathematical Society, 2005.
- [14] Thomas G. Wright and Lloyd N. Trefethen. Large-scale computation of pseudospectra using arpack and eigs. *SIAM Journal on Scientific Computing*, 23(2):591–605, 2001.
- [15] Thomas G. Wright. Eigtool: A graphical tool for nonsymmetric eigenproblems, 2002. MATLAB software package available at <http://www.comlab.ox.ac.uk/pseudospectra/eigtool>.
- [16] Diederich Hinrichsen and Anthony J. Pritchard. *Mathematical Systems Theory I: Modelling, State Space Analysis, Stability and Robustness*, volume 48 of *Texts in Applied Mathematics*. Springer, Berlin, 2005.
- [17] Brian F. Farrell and Petros J. Ioannou. Generalized stability theory. part i: Autonomous operators. *Journal of the Atmospheric Sciences*, 53(14):2025–2040, 1996.
- [18] Thomas Braconnier and Nicholas J. Higham. Computing the field of values and pseudospectra using the lanczos method with continuation. *BIT Numerical Mathematics*, 36(3):422–440, 1996.
- [19] S. H. Lui. Computation of pseudospectra by continuation. *SIAM Journal on Scientific Computing*, 18(2):565–573, 1997.
- [20] Gene H. Golub and Charles F. Van Loan. *Matrix Computations - 4th Edition*. Johns Hopkins University Press, Philadelphia, PA, 2013.
- [21] Nicholas J. Higham. *Accuracy and Stability of Numerical Algorithms*. Society for Industrial and Applied Mathematics, second edition, 2002.
- [22] Friedrich L. Bauer and Charles T. Fike. Norms and exclusion theorems. *Numerische Mathematik*, 2:137–141, 1960.
- [23] Matthew Tancik, Pratul P. Srinivasan, Ben Mildenhall, Sara Fridovich-Keil, Nithin Raghavan, Utkarsh Singhal, Ravi Ramamoorthi, Jonathan T. Barron, and Ren Ng. Fourier features let networks learn high frequency functions in low dimensional domains. In *Advances in Neural Information Processing Systems (NeurIPS)*, 2020.
- [24] Kaiming He, Xiangyu Zhang, Shaoqing Ren, and Jian Sun. Deep residual learning for image recognition. In *2016 IEEE Conference on Computer Vision and Pattern Recognition (CVPR)*, pages 770–778, 2016.
- [25] Prajit Ramachandran, Barret Zoph, and Quoc V. Le. Searching for activation functions. *ArXiv*, abs/1710.05941, 2017.
- [26] Haibo He and Eduardo A. Garcia. Learning from imbalanced data. *IEEE Transactions on Knowledge and Data Engineering*, 21(9):1263–1284, 2009.
- [27] Mateusz Buda, Atsuto Maki, and Maciej A. Mazurowski. A systematic study of the class imbalance problem in convolutional neural networks. *Neural Networks*, 106:249–259, 2018.
- [28] Diederik P. Kingma and Jimmy Ba. Adam: A method for stochastic optimization. *CoRR*, abs/1412.6980, 2014.

- [29] M.J. Berger and P. Colella. Local adaptive mesh refinement for shock hydrodynamics. *Journal of Computational Physics*, 82(1):64–84, 1989.
- [30] J.P. Serra and J. Serra. *Image Analysis and Mathematical Morphology*. Image analysis and mathematical morphology. Academic Press, 1982.
- [31] R.M. Haralick and L.G. Shapiro. *Computer and Robot Vision*. Number v. 1 in Computer and Robot Vision. Addison-Wesley Publishing Company, 1992.